Harnessing Nonuniform Pressure Distributions in Soft Robotic Actuators

*Yoav Matia, Gregory H. Kaiser, Robert F. Shepherd, Amir D. Gat, Nathan Lazarus, and Kirstin H. Petersen**

Herein, complex motion in soft, fluid-driven actuators composed of elastomer bladders arranged around a neutral plane and connected by slender tubes is demonstrated. Rather than relying on complex feedback control or multiple inputs, the motion is generated with a single pressure input, leveraging viscous flows within the actuator to produce nonuniform pressure between bladders. Using an accurate predictive model coupling with a large deformation Cosserat rod model and low-Reynolds-number flow, all dominating dynamic interactions including extension and curvature are captured with two governing equations. Given insights from this model, five design elements are described and demonstrated in practice. By choosing the relative timescales between the solid, fluid, and input pressure cycles, the tip of the actuator can obtain almost any desired trajectory and can be placed anywhere temporarily within its 2D workspace. Finally, the benefits of viscous-driven soft actuators are showcased in a six-legged untethered robot able to walk 0.05 body lengths per second. The foundation is laid for a new class of morphologically intelligent, soft robotic actuators that enables complex deformations and multifunctionality without explicit drivers; whereby generating nonuniform pressure distributions, their infinite degrees of freedom can be exploited.

1. Introduction

Fluidic elastomer actuators (FEAs) feature large relative deformations, infinite degrees of freedom, and passive adaptation to external perturbations, despite minimalist designs and inexpensive fabrication techniques. These remarkable properties have led to widespread adoption in biomedical devices,[1] factory and field manipulation,[2] wearables,[3] and mobile aqueous, airborne, and ground robots.[4,5] A key to their success is morphological intelligence that enables complex deformations and multifunctionality without explicit control signals paving the way for cost-effective robots that can be deployed in greater numbers and across different size scales. Such minimal soft mechanisms may work independently or complement more sophisticated control architectures for a higher degree of versatility.

In pursuit of a larger workspace, and better control and resolution within that workspace, researchers have introduced strain-limiting layers,[6] antagonistic configurations,[7] addressable bang-bang control of pumps and valves,[8] negative pressures,[9,10] and use of external obstacles to induce deformations.[11] In recent years, researchers have also shown new ways to achieve minimalist control, either by passive pressure-driven valves to produce actuator oscillations,[12] or by bringing utility to fluid viscosity through narrow internal channels that connect elastomer bladders,[13,14] stochastic pore distribution,[15] or viscous peeling.[16] In a similar vein, viscous controllers have been shown to be able to drive a delay sequence of single mode, constant curvature FEAs.[17]

In spite of this progress, the field has yet to demonstrate complex actuation profiles with practical drive circuitry, on par

---

Y. Matia
College of Engineering
Cornell University
Ithaca, NY 14853, USA

Y. Matia
ORAU Fellowship Program at Army Research Lab
Adelphi, MD 20783, USA

The ORCID identification number(s) for the author(s) of this article can be found under https://doi.org/10.1002/aisy.202200330.

DOI: 10.1002/aisy.202200330

G. H. Kaiser, R. F. Shepherd, K. H. Petersen
College of Engineering
Cornell University
Ithaca, NY 14853, USA
E-mail: kirstin@cornell.edu

A. D. Gat
Mechanical Engineering
Technion - Israel Institute of Technology
Technion City, Haifa 3200003, Israel

N. Lazarus
Electrical and computer engineering
University of Delaware
139 The Green, Newark, DE 19716, USA

with the infinite passive degrees of freedom that are the hallmark of soft actuators. Toward this goal, we cast FEAs in a new light. Fundamentally, the primary two-way coupled mechanism governing all FEAs is the balance between the spatial change in flux and the volume change. This change in flux is related to spatial pressure gradients in the fluid field that generate stresses on the fluid–solid interface; these stresses, in turn, produce local moments and normal forces in the solid, which deform the actuator and vice versa. In these fluid-structure dynamics, we identify three governing timescales: the elastic-inertial timescales of the solid t_s^*, the viscous-elastic timescale of the fluid t_f^*, and the input transient timescale t_i^*.

Following this insight, we map out previous state-of-the-art soft-robots along two axes (**Figure 1**), where the x-axis represents a measure of the fluidic spatial pressure distribution and the *y*-axis the degree of solid inertia. Along the *x*-axis, we see that for $t_\mathrm{s}^*/t_\mathrm{f}^* \ll 1$, quadrants (II) and (III), pressure propagates significantly slower than solid impulse response, solid inertia becomes negligible, and the FEA reflects spatial variations in the fluidic pressure field. For $t_\mathrm{s}^*/t_\mathrm{f}^* \gg 1$, quadrants (I) and (IV), fluidic pressure propagates significantly faster than the solid response to pressure gradients, and the FEA behaves as if it is responding to a uniform spatial pressure distribution. Along the y-axis, we see that for $t_\mathrm{s}^*/t_i^* \ll 1$, quadrants (III) and (IV), solid-field impulse response is significantly faster than the input signal transient and the FEA has a quasistatic transient behavior. In contrast, for $t_\mathrm{s}^*/t_i^* \gg 1$, quadrants (I) and (II), the input signal transients dominate, and the FEA has either an inertial response or a quasistatic response, based on pressure propagation rates $t_\mathrm{s}^*/t_\mathrm{f}^* \gg 1$ or $t_\mathrm{s}^*/t_\mathrm{f}^* \ll 1$, respectively.

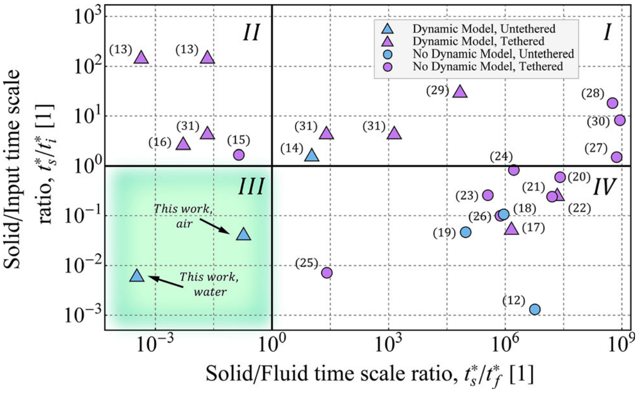

Figure 1. Characterization of the state of the art in soft robotics and how this contribution differentiates itself. The *x*-axis depicts a measure of fluidic spatial pressure distribution in the form of a ratio between the elastic-inertial timescales t_s^* over the viscous-elastic timescale t_f^*. In the y-axis, we present a measure of solid inertia involvement, expressed as a ratio of the elastic-inertial timescales t_s^* over the input signal transient timescale t_i^*. The domain space has been divided into four quadrants based on their unique characteristics: I) uniform spatial pressure quadrant, dominated by solid inertia. II) Spatial pressure distribution dominated quadrant, with steep input transient times. III) Spatial pressure distribution dominated quadrant, with fluid timescale input transient times. IV) Uniform spatial pressure quadrant exhibiting quasistatic transient behavior. The work highlighted in this plot is further detailed in Appendix A, Supporting Information.

"Classic" FEAs predominantly occupy quadrant (IV),[12,17–26] where a spatially uniform pressure distribution is coupled with quasistatic transient behavior. Recent work on dynamic response and combustion-driven FEAs falls in quadrant (I),[14,27–31] where a spatially uniform pressure distribution (as $t_\mathrm{s}^*/t_i^* \gg 1$) and solid inertia dominate. Here, the uniform pressure-to-curvature (stress–strain) characteristics of the material restrict the FEA to one spatiotemporal pattern with a decaying inertial transient superimposed upon it. For both quadrants, the FEA forms a semicircular deformed state since all sections exhibit the same pressure-to-curvature profile and experience the same pressure. Circumventing this can only be achieved by adding complexity, such as patterning structural asymmetries, or external control schemes, such as discretized section controls.

Quadrant (II) is more sparsely studied and occupied mainly by theoretical work. Work in this quadrant is dominated by the spatial pressure distribution with steep input transient times.[13,15,16,31] Deformation includes localized sharp pressure gradients as $t_\mathrm{s}^*/t_i^* \gg 1$, which result in pseudo-inertial, yet diffusivity-decaying deformation propagating down the length of the FEA.

Our work is the first to suggest operation in quadrant (III), where the spatial pressure distribution and the fluid-scale input transient times dominate. Here, deformation is driven by spatial pressure variations and fluid-scale temporal input gradients that are insufficient to evoke a leading-order inertial response at the solid. This unique combination gives rise to varying spatiotemporal deformation patterns, even when driven by a single input pressure profile. Specifically, in this paper, we introduce both theory and experiments to achieve complex motion in FEAs by leveraging viscous flows which cause nonuniform pressure distributions throughout the actuator. We show how to generate multiple deformation shapes and amplitudes (the spatial part) with time-varying form and position in space (the temporal part), and do so independently of patterning structural asymmetries or complex control schemes.

We start from the traditional approach whereby asymmetry in stress about the neutral plane of the solid body produces curvature, whereas symmetry induces axial deformation. Next, we construct the simplest possible unit cell of soft fluid-driven actuators, namely a closed series of evenly distributed cavities embedded in elastomer bellows, and pressurize them through slender tubes. Finally, we embed the control mechanism within the structure itself, in the form of preconfigured interconnections, as depicted in the configuration schematic (**Figure 2**A).

If such an actuator was operated in Quadrant (IV) and driven by a single pressure inlet, the tip could be placed vertically. If it was driven antagonistically with a separate pressure source per column, the tip could be placed in a 2D workspace. Whereas it would take a separate pressure source per bellow to achieve full control. Operation in Quadrant (III) enables an important subset of the latter, through a single pressure inlet. Here, a stable inlet pressure can be used to position the tip of the actuators vertically similar to classic FEAs, but a changing inlet pressure can be used to drive both the tip and the profile of the actuator in complex trajectories. We see this, for example, in Figure 2B,C where we show four distinct, tracked tip motion cycles that would otherwise be impossible to achieve without at least two pressure

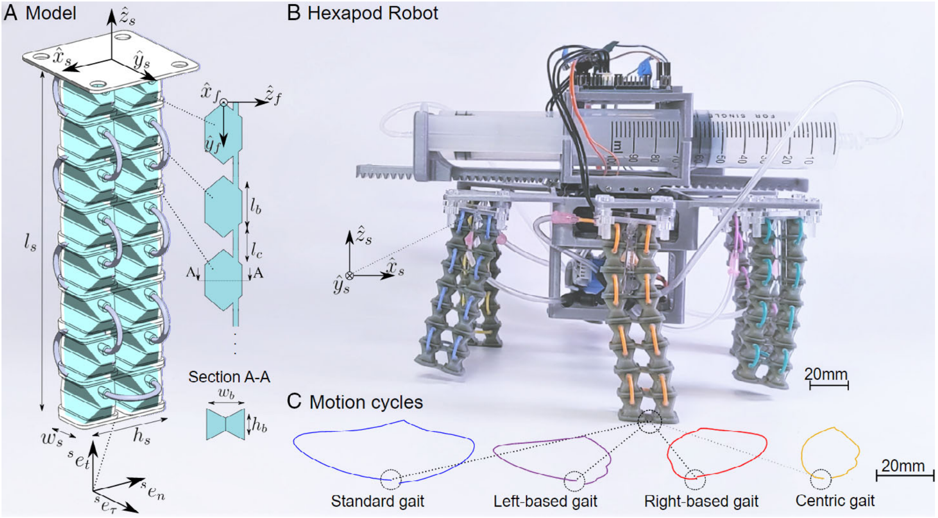

Figure 2. A) Sketch of a single actuator (left), composed of a closed system of fluid-filled bellows and interconnecting tubes, alongside a sketch showing the internal geometry as experienced by the fluid (marked in turquoise). B) Hexapod robot walking with two sets of three viscous-driven actuators coupled in parallel, driven only by two syringe pumps. Note that all motion occurs in the $(\hat{x}_s, \hat{z}_s)$-plane. C) Example motion cycles caused by different inlet pressure profiles.

sources or more complex driver circuitry. Note also that the snapshot of the robot illustrates actuator profiles that would be impossible to achieve with two separately driven antagonistic elastomer cavities. In this article, we focus exclusively on demonstrating the potential of this new operating regime. However, this design technique does not restrict combination with more traditional methods; for example, valves can be added to permit the two columns of bellows to also be driven antagonistically.

We provide a compact predictive model that couples large deformation, modeled by a Cosserat rod continuum, with low-Reynolds-number flow in the slender tubes, capturing leading-order dynamic interactions, including extension and flexure. Following insights from this model, and to make this new design space more accessible to experimentalists, we categorize these interactions into five dominant mechanisms and provide illustrations of their influence in practice (Figure 3, 4 and Movie S1–5, Supporting Information).

We further demonstrate the use of these mechanisms in a six-legged robot driven by two onboard syringe pumps (Figure 2B, 5 and Movie S6, Supporting Information). Guided by the model and the experimentally derived parameters, we are able to achieve speeds of 0.05 body lengths per second (BL s^{-1}). It is worth noting that this is on the order of the most prominent existing examples of soft, fluid-driven, legged, untethered robots,[12,19] in spite of the fact that we inherently introduce delays in our system by relying on viscous-driven pressure differentials, rather than explicit driver circuitry as in classic FEAs. As highlighted by blue markers in Figure 1, such untethered walking robots supported by theoretical frameworks are rare due to the high pressures and consequently high payloads required to achieve significant motion. Beyond serving as a powerful demonstration, our robot implementation elucidates the relation between absolute pressure and payload and stability.

Our goal with this paper is to provide, for the first time, a reduced model and a meaningful experimental demonstration to equip the reader with a toolset to harness the full potential of the fluid–structure interaction internal to viscous fluid-driven soft robots, empowering them to generate their own complex spatiotemporal deformations previously unattainable without extensive external control.

2. Analysis

2.1. Model Derivation

Here, we formulate the theoretical framework for a two-way coupled fluid–structure interaction reduced physical model, as well as respective characteristic scales, describing the nonlinear dynamics of viscous fluid-driven soft robots based on ref. [14]. We present the fundamental steps required to reconstruct the model tailored to the actuators used throughout this paper. The model is intended to provide the reader with key insights into the governing mechanism of such systems and provide a practical goal-oriented design tool and predictor for the dynamic behavior of such systems. We start from the traditional approach whereby asymmetry in stress about the neutral plane of the solid body produces curvature, whereas symmetry induces axial deformation. We distribute a matrix of interconnected fluid-filled bladders evenly about the neutral plane and pressurize them. The pressure within the fluid-field generates and is induced by deformation of the solid structure. In Figure 2A, we present the fundamental configuration in use.

We denote vector variables using bold letters, direction vectors by hat notation, nondimensional variables by tilde or capital letters, characteristic values by asterisk superscript, and s or f subscripts for solid or fluid properties, respectively. For a full nomenclature, scaling arguments, and detailed characteristic scale, see Appendix Section B.1 and Table B.1, Supporting Information. We define a lab frame of reference $(\hat{x}_s, \hat{y}_s, \hat{z}_s)$ for the solid domain with a dimensional curvilinear length coordinate θ along the actuator's reference curve (neutral axis), and assign a position vector $x = (x(\theta, t), z(\theta, t))$ pointing to the material point along it. We define a fluidic-field bladder-tube curvilinear frame $(\widehat{x}_\mathrm{f}, \widehat{y}_\mathrm{f}, \widehat{z}_\mathrm{f})$ defined such that $\widehat{x}_\mathrm{f}$ is the streamwise direction, perpendicular to the $\widehat{y}_\mathrm{f} - \widehat{z}_\mathrm{f}$ plane. We define actuator length l_s, height h_s, width w_s, Young's modulus E, solid density ρ_s, and parameters f_e, f_i as solid-field correction coefficients for cross sectional extension and bending stiffness, comparing the actuator to a full rectangular cross-section beam with identical dimensions, see Appendix Section B.5, Supporting Information. Frames of reference and geometric dimensions are illustrated in Figure 2A.

We limit our analysis to a beam-like configuration dominated by viscous fluid-filled bladders $w_\mathrm{b}/l_\mathrm{s} \ll 1$. The averaged properties of these "unit cells" can be used to approximate that of the solid domain's averaged property as $(w_\mathrm{b} \cdot n/2)/l_\mathrm{s} \sim 1$, where $n/2$ is the number of bladders along the actuator length l_s. We examine the 2D deformation in the $\widehat{x}_\mathrm{s} - \widehat{z}_\mathrm{s}$ plane considering only directors $(d_1(\theta, t), d_3(\theta, t))$. The explicit representations of relevant directors of the lab frame in dimensional form are $d_1 = ((\partial z_\mathrm{s})/(\partial \theta), -(\partial x_\mathrm{s})/(\partial \theta))$ and $d_3 = ((\partial x_\mathrm{s})/(\partial \theta), (\partial z_\mathrm{s})/(\partial \theta))$.

We define a small parameter representing the slenderness of the fluidic domain $\varepsilon_1 = 2r_\mathrm{c}/l \ll 1$, where r_c is the tube radius and l is the total length of connective array of tubes. Next, we formulate the Stokes equations for incompressible, creeping, Newtonian flow in a slender elastic domain. The resulting conservation of momentum is $\nabla p = \mu \nabla^2 u$, and the conservation of mass $\nabla \cdot u = 0$ with pressure p, the flow-field velocity u, and the fluid dynamic viscosity μ. Applying order-of-magnitude analysis, and implementing lubrication and Gauss theorem, we integrate over conservation of mass and obtain a nonlinear diffusion equation balancing the change in axial flux with the change in cross section over time in nondimensional terms

$$\underbrace{-\left(\frac{\partial^2 P}{\partial X_f^2} \cdot Q_1 + \frac{\partial P}{\partial X_f} \cdot \left(\frac{\partial Q_1}{\partial X_f}\right)\right)}_{\text{Change in axial flux}} + \underbrace{\frac{\partial A}{\partial P}\frac{\partial P}{\partial T}}_{\text{unsteady pressure term}} + \underbrace{\left(R\frac{\partial A}{\partial \tilde{M}_e}\frac{\partial \tilde{M}_e}{\partial T} + |(R)|\frac{\partial A}{\partial \tilde{N}_e}\frac{\partial \tilde{N}_e}{\partial T}\right)}_{\text{change in fluid section due to resultant from solid domain}} = 0 \tag{1}$$

In governing Equation (1), we see how the axial flux is diffusive in nature as evident by the nondimensional permeability $Q_1 = Q_1^\mathrm{b}\Gamma_\mathrm{Q}(X_\mathrm{f})$, where the advective term $\partial P/\partial X_\mathrm{f}$ only contributes the nondimensional pressure $P = p/E$ propagation in the presence of a permeability gradient along the length of the fluid field (as it is in our case where bladders and connective tubing have a nonuniform cross section). Balancing the axial flux is the change in cross section $A = a/a_0^* = a/\pi r_\mathrm{c}^2$ over time $T = t/t_\mathrm{f}^*$ as given by our unsteady pressure term and $\partial A/\partial P = (\partial A_\mathrm{p1}/\partial P)\Gamma_\mathrm{A}(X_\mathrm{f})$ representing the change in cross section per unit pressure, and the feedback source terms from the solid-field resultants for normal force $\tilde{N}_\mathrm{e}$, and moment $\tilde{M}_\mathrm{e}$ via $\partial A/\partial \tilde{N}_\mathrm{e} = (\partial A_{N1}/\partial \tilde{N}_\mathrm{e})\Gamma_\mathrm{A}(X_\mathrm{f})$, $\partial A/\partial \tilde{M}_\mathrm{e} = (\partial A_\mathrm{M1}/\partial \tilde{M}_\mathrm{e})\Gamma_\mathrm{A}(X_\mathrm{f})$ coupling solid-field deformation to flow. Last, we differentiate between the parametric value referring to bladder or tube by setting

$$\Gamma_\mathrm{A}(X_\mathrm{f}) = \begin{cases} \dfrac{\partial \Theta(x_\mathrm{f})}{\partial X_\mathrm{f}} = 0, 1 \\ \dfrac{\partial \Theta(x_\mathrm{f})}{\partial X_\mathrm{f}} \neq 0, 0 \end{cases} \tag{2}$$

$$\Gamma_\mathrm{Q}(X_\mathrm{f}) = \begin{cases} \dfrac{\partial \Theta(x_\mathrm{f})}{\partial X_\mathrm{f}} = 0, 1 \\ \dfrac{\partial \Theta(x_\mathrm{f})}{\partial X_\mathrm{f}} \neq 0, Q_1^\mathrm{c}/Q_1^\mathrm{b} \end{cases} \tag{3}$$

with bladder permeability Q_1^b and connective tube's Q_1^c respective to X_f position. In providing the feedback from solid to fluid field, we define $\Theta(X_\mathrm{f})$ as the coordinate mapping function of solid-field deformation onto the fluidic pressure field. For more detail, see Appendix Section B.3.5 and B.7, Supporting Information. The pressure source terms in Equation (1) are governed by $\partial \tilde{M}_\mathrm{e}/\partial T$ and $\partial \tilde{N}_\mathrm{e}/\partial T$. We thus need to map our resultants onto the fluid field to derive their respective values. Even for large deformations, leading-order predictions can be achieved with good agreement by setting $\partial A_\mathrm{p1}/\partial P = (E/a_0^*) \cdot \partial a_1/\partial p$, $\partial A_{N1}/\partial \tilde{N}_\mathrm{e} = (N_\mathrm{e}^*/a_0^*) \cdot \partial a_1/\partial N_\mathrm{e}$, and $\partial A_\mathrm{M1}/\partial \tilde{M}_\mathrm{e} = (V_\mathrm{e}^* l_\mathrm{s}/a_0^*) \cdot \partial a_1/\partial M_\mathrm{e}$ as averaged constants (**Figure 3**). To enhance the prediction capabilities of the model for systems whose response to pressure and external forces is significantly nonlinear due to hyperelasticity, these can be readily replaced with curve-fitted functions, measured from the material.[14] Finally, we define $R(X_\mathrm{f}) = 1$ and $R(X_\mathrm{f}) = -1$ discretely to indicate to which column within the actuator the bladder belongs.

Over the solid domain, we consider the dynamics of this FEA, or elastic beam, initially at rest. We set an intrinsic Cosserat rod formulation nondimensional deflection U_1 and extension U_3 in the x_s and z_s direction, respectively. We limit the cross section to maintain its initial shape and remain perpendicular to the reference curve based on the assumption of negligible cross-sectional extension, cross-sectional shear, and tangential shear; finally, we obtain the reduced nondimensional form respective to the X_s and Z_s direction

$$\underbrace{\tau^2\begin{pmatrix} \partial^2 U_1/\partial T^2 \\ \partial^2 U_3/\partial T^2 \end{pmatrix}}_{\text{Linear inertia}} = \underbrace{\begin{pmatrix} B_x \\ B_z \end{pmatrix}}_{\text{Traction}} + \underbrace{\left[\eta\frac{\partial \tilde{N}_\mathrm{e}}{\partial \Theta} - \tilde{\alpha}_\mathrm{e}\tilde{V}_\mathrm{e}\right]\begin{pmatrix} E_{tx} \\ E_{tz} \end{pmatrix}}_{\text{Curvilinear tangential force}} + \underbrace{\left[\frac{\partial \tilde{V}_\mathrm{e}}{\partial \Theta} + \eta\tilde{\alpha}_\mathrm{e}\tilde{N}_\mathrm{e}\right]\begin{pmatrix} E_{nx} \\ E_{nz} \end{pmatrix}}_{\text{Curvelinear normal force}} + \underbrace{\frac{\partial}{\partial \Theta}\left[\frac{1}{d_{33}}\begin{pmatrix} \left(B_x^1 - Y^{11}\tau^2\frac{\partial^2 \tilde{d}_{1x}}{\partial T^2}\right)\tilde{d}_{3x} \\ +\left(B_z^1 - Y^{11}\tau^2\frac{\partial^2 \tilde{d}_{1z}}{\partial T^2}\right)\tilde{d}_{3z} \end{pmatrix}\begin{pmatrix} \tilde{d}_{1x} \\ \tilde{d}_{1z} \end{pmatrix}\right.}_{\text{Rotary inertia}} \tag{4}$$

where $\tilde{V}_\mathrm{e}$ is the nondimensional shear force resultants and Θ is the nondimensional curvilinear length coordinate along the beam reference curve. We define our kinematic variable for curvature $\tilde{\alpha}_\mathrm{e}$, the structure reference curve tangent

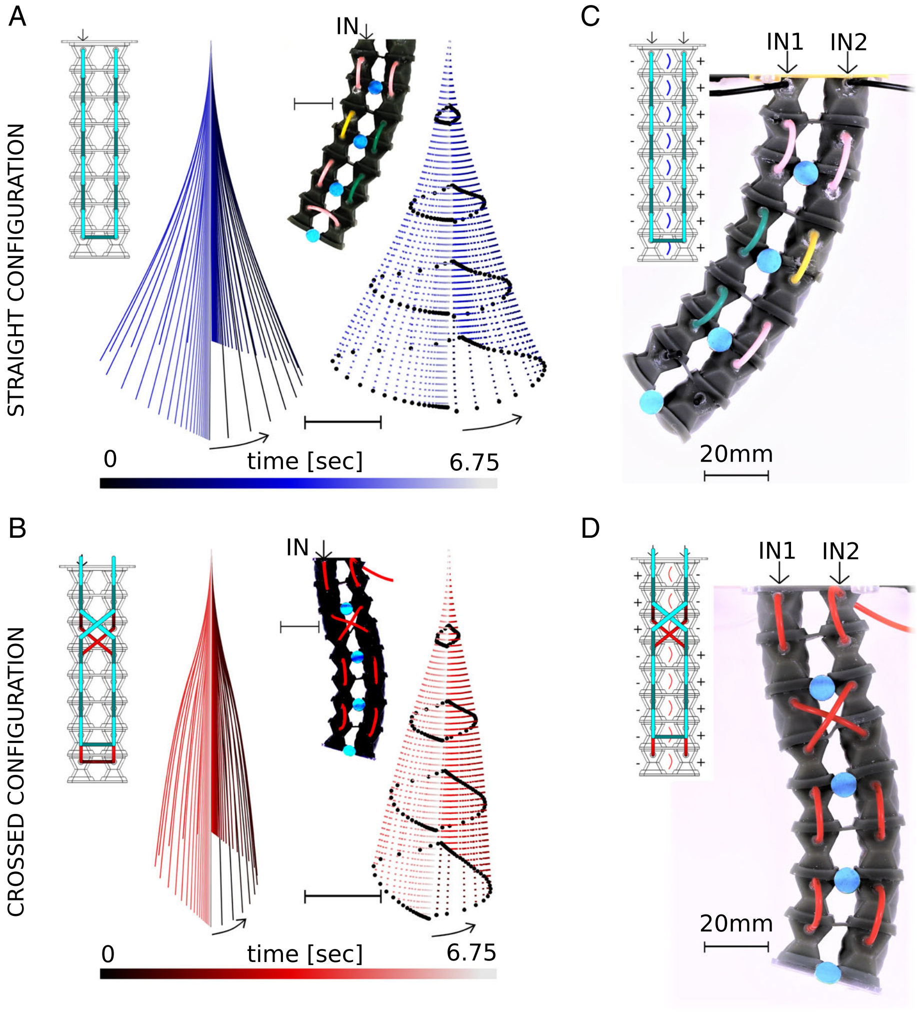

Figure 3. A,B) Similar input pressure profiles lead to different transient behavior when the actuators are configured in a straight or crossed configuration, also shown in the inserts on the top left. Notice that these actuators only have a single pressure inlet. Solid lines are motions predicted by the model; black marks are tracked markers in footage of the real leg, the colored dots are splines fitted to those marks. Curve color indicates passing of time; similarly, the position of markers indicate both the spatial and temporal position of the actuator. All scale bars indicate 20 mm. Both experimental and predictive model curves use the same inlet pressure profile $P(0,T) = P_{\max} - \Delta P_{\max}/(1+\exp(-2\kappa(T-0.5/t_f^*))) + \Delta P_{\max}/(1+\exp(-2\kappa(T-4/t_f^*)))$. For more information, see section 2 under fluid-field boundary conditions, and Appendix Section C.6, Supporting Information. C,D) Steady-state configuration of the actuator under positive pressure, with two different configurations.

$E_t = (\tilde{d}_{3x}, \tilde{d}_{3z})/\tilde{d}_{33}^{1/2}$, and normal $E_n = -(\tilde{d}_{1x}, \tilde{d}_{1z})/\tilde{d}_{33}^{1/2}$ components with the nondimensional directors being

$$\tilde{d}_1 = (1+\partial U_3/\partial\Theta, \; -\partial U_1/\partial\Theta), \; \tilde{d}_3 = (\partial U_1/\partial\Theta, 1+\partial U_3/\partial\Theta) \quad \text{and} \quad \tilde{d}_{33} = \tilde{d}_3 \cdot \tilde{d}_3 \tag{5}$$

We notice the emergence of three critical nondimensional numbers determining the dynamic regime of the structure: the timescale ratio $\tau = t_s^*/t_f^*$ where $t_s^* \sim \sqrt{m l_s^4/EIf_i}$ is the elastic-inertial timescale and $t_f^* \sim \mu(\partial a_1/\partial p)|_{p=p_0}/(a_0^* \varepsilon_1^2)$ is the viscous-elastic timescale, the normalized squared radius of gyration $Y^{11} = (If_i)/(w_s h_s f_m l_s^2)$, and the force scale ratio determining the balance between shear and normal forces $\eta = N_e^*/V_e^* = E h_s w_s f_e/(E w_s h_s^3 f_i/(12 l_s^2))$. Last, we define the nondimensional distributed traction force per unit mass $B = (B_x, B_z) = (b_x/(V_e^*/l_s m), \eta b_z/(V_e^*/l_s m))$ and the nondimensional distributed moment per unit mass vectors $B^1 = (B_x^1, B_z^1) = (b_x^1/(V_e^*/m), \eta b_z^1/(V_e^*/m))$. Finishing the explicit form of the reduced model, we provide the constitutive laws coupled with feedback from the fluidic domain pressure P

$$\tilde{N}_e = (\tilde{\lambda}_e - 1) \tag{6}$$

$$\tilde{M}_e = \tilde{\alpha}_e \tag{7}$$

$$\tilde{V}_e = -\frac{1}{\tilde{d}_{33}^{1/2}} \frac{\partial \tilde{M}_e}{\partial \Theta} \tag{8}$$

With respective fluid coupled intrinsic kinematic variables

$$\underbrace{\tilde{\lambda}_e}_{\text{Elastic stretch}} = \underbrace{\frac{1}{\lambda_{\mathrm{e}}^{*}}\tilde{d}_{33}^{1/2}}_{\text{Overall stretch}} - \underbrace{\frac{\lambda_{\mathrm{p}}^{*}}{\lambda_{\mathrm{e}}^{*}}\overline{P}(X_{\mathrm{f}})\phi\frac{\partial\zeta}{\partial(\overline{p}/E)}}_{\text{Pressure}-\text{based stretch}} \tag{9}$$

$$\underbrace{\tilde{\alpha}_{\mathrm{e}}}_{\text{Elastic curvature}} = \underbrace{\frac{1}{l_{\mathrm{s}}^{2}}\frac{\tilde{d}_{1x,3}\tilde{d}_{3x}+\tilde{d}_{1z,3}\tilde{d}_{3z}}{\tilde{d}_{33}^{1/2}}}_{\text{Overall curvature}} + \underbrace{\frac{\alpha_{\mathrm{p}}^{*}}{\alpha_{\mathrm{e}}^{*}}P'(X_{\mathrm{f}})\Phi\frac{\partial\psi}{\partial(p'/E)}}_{\text{Pressure}-\text{based curvature}} \tag{10}$$

where the effective normalized pressure for slope and extension generation are respectively $P'(X_{\mathrm{f}}) = (P_{\mathrm{d}}(X_{\mathrm{f}}) - P_{\mathrm{u}}(X_{\mathrm{f}}))$ and $\overline{P}(X_{\mathrm{f}}) = (P_{\mathrm{d}}(X_{\mathrm{f}}) + P_{\mathrm{u}}(X_{\mathrm{f}}))$, where P_{u} and P_{d} are the fluidic pressures at the right and left bladders, $\partial\zeta/\partial(\overline{p}/E)$ is the dimensional change in length per cross-section per normalized pressure sum, and $\partial\psi/\partial(p'/E)$ represents the change in beam slope per cross section per normalized pressure difference. The coupling introduces the fluid pressure as a source term for curvature and extension per solid domain coordinate Θ. Defining these terms requires us to map our fluidic domain solution using the $X_{\mathrm{f}}(\Theta)$ mapping, for more detail, see Appendix Section B.3.5 and B.6, Supporting Information. Last, we note the characteristic measures for curvature $\alpha_{\mathrm{e}}^{*}{\sim}\alpha_{\mathrm{p}}^{*}{\sim}1/l_{\mathrm{s}}$ and stretch $\lambda_{\mathrm{e}}^{*}{\sim}\lambda_{\mathrm{p}}^{*}{\sim}1$, where the subscripts e represent the source of the measure being external forces, that is, traction applied to the surface, and the subscript p represent pressure.

Concluding our model, we set the boundary and initial conditions for a well-posed problem. Both fluid and solid fields start from rest. For the solid field, we set standard boundary conditions for a cantilever beam; over the fluid field, we set $P(0,T) = P_{\max} - \Delta P_{\max}/\left(1+\exp\left(-2\kappa\left(T-0.5/t_{\mathrm{f}}^{*}\right)\right)\right) + \Delta P_{\max}/\left(1+\exp\left(-2\kappa\left(T-4/t_{\mathrm{f}}^{*}\right)\right)\right)$ as the pressure input signal where the maximum pressure is $P_{\max} = 0.02245$, the total pressure difference $\Delta P_{\max} = 0.0785$, and the sigmoid logistic growth rate $\kappa = (6/\delta_{\mathrm{T}})$ with $\delta_{\mathrm{T}} = t_{i}^{*}/t_{\mathrm{f}}^{*} = 0.875/t_{\mathrm{f}}^{*}$ as the nondimensional transition period between the upper and lower pressure limits. The experimental procedure to obtain the inlet function is detailed in Appendix Section C.6, Supporting Information. Last, we define the far-end of the bladder-tube array as sealed by setting $(\partial P(X_{\mathrm{f}},T)/\partial X_{\mathrm{f}})|_{X_{\mathrm{f}}=1} = 0$.

In Experimental Section, we quantify the parameters of our experimental system for use with this model and in Appendix Section C.1–5, Supporting Information, we detail how the following five coupling coefficients were measured: 1) the change in bladder cross section per unit pressure, 2) the change in actuator slope per cross section per normalized pressure difference, 3) the change in actuator length per cross section per normalized pressure sum, 4) the change in bladder cross section per normal force resultant, and 5) the change in bladder cross section per moment resultant. Having defined those, we can calculate both the inertial-elastic timescale $t_{\mathrm{s}}^{*}{\sim}\sqrt{(ml_{\mathrm{s}}^{4}/EIf_{i})} = 0.029[\mathrm{sec}]$ and the viscous-elastic timescale $t_{\mathrm{f}}^{*}{\sim}\mu(\partial a_{1}/\partial p)|_{p=p_{0}}/\left(a_{0}^{*}\varepsilon_{1}^{2}\right) = 0.157[\mathrm{sec}]$. Next, we reason about five intuitive mechanisms derived from the reduced model formulated earlier and experimentally demonstrate each independently. These, when superimposed, provide a complete toolset to guide goal-oriented design of complex viscous-driven motion cycles in FEAs.

3. Results

Having defined a theoretical predictive model, we identify five mechanisms within our control and demonstrate how various scaling arguments can be used to formulate design principles for viscous flow–driven robotic limbs, namely the spatial distribution of connected bladders, the viscous-elastic to inertial elastic timescale ratio, the viscous-elastic to input timescale ratio, the mass flux control via viscous resistance, and the cycled baseline pressure. See Movie S1–5, Supporting Information, for real-time recordings of the actuator motion cycles and examples of each of these mechanisms.

3.1. Spatial Distribution of Connected Bellows

The system's dynamics are affected by the spatial distribution of bladders. Recall Equation (1), which shows how lag resulting from the diffusive propagation of pressure provides an advantage in generating complex transient deformation patterns with a single input in a closed system. Figure 3A,B and Movie S1, Supporting Information, illustrate the concept: two actuators with an identical pressure inlet (For more information, see Section 2 under fluid-field boundary conditions, and Appendix Section C.6, Supporting Information), but different connectivity, will exhibit significantly different spatiotemporal motion. The straight connectivity produces wide motion, whereas a single crossing of connections produces narrower cycles. Similarly, the profile of the actuator throughout the motion cycle differs, as does the slope of the actuator tip. In a legged-robot gait, this could be equated to ostrich-like strides and elephant-like trot respectively. While the trajectory of the tip of actuator may appear qualitatively similar, the difference in curvature throughout the motion cycle in the FEA causes significantly different tip angles.

Using numerical solutions of the coupled system of governing Equation (1) and (4), we observe a good agreement between the predictive model and experimental curves of the actuator's dynamic behavior, see Figure 3A,B, left versus right. The model predicts the initial extension within 2.8% and 3.2% of the actual extension in the straight and crossed configuration, respectively, and the maximum horizontal deflection within 4.7% and 12.6% of the actual deflection for the straight and crossed configuration, respectively.

Last, we show a way to determine the initial steady state of the actuator in Figure 3C,D. The diagram shows the positive and negative pressurized bellows in relation to the neutral plane with a plus or minus sign corresponding to the inlet pressure. A bellow pair with a $(+)-(-)$ will bend to the right, $(-)-(+)$ to the left, $(+)-(+)$ will extend, and $(-)-(-)$ will contract. This corresponds to the characterized values for the change in actuator angle per unit per normalized pressure, $\partial\psi/\partial(p'/E)$, and change in actuator length per unit per normalized pressure, $\partial\zeta/\partial(\overline{p}/E)$, respective to the pressure difference $P'(X_{\mathrm{f}}) = P_{\mathrm{d}}(X_{\mathrm{f}}) - P_{\mathrm{u}}(X_{\mathrm{f}})$ and pressure sum $\overline{P}(X_{\mathrm{f}}) = P_{\mathrm{d}}(X_{\mathrm{f}}) + P_{\mathrm{u}}(X_{\mathrm{f}})$.

3.2. Solid and Fluid Timescale Ratio

The viscous-elastic to inertial elastic timescale ratio is an instrumental characteristic scale for determining the dynamic regime in which our system operates

$$\tau = t_{\mathrm{s}}^{*}/t_{\mathrm{f}}^{*} = \underbrace{\sqrt{(m l_{\mathrm{s}}^{4}/EIf_{i})}}_{\text{Inertial}-\text{elastic time scale}} \Big/ \underbrace{(\mu(\partial a_1/\partial p)|_{p=p_0}/(a_0^{*}\varepsilon_1^{2}))}_{\text{Viscous}-\text{elastic time scale}} \tag{11}$$

In Figure 4 and Movie S2, Supporting Information, we show how we can switch between actuation modes solely based on the dynamic regime. The magenta dashed curve in **Figure 4A** shows a water-filled system, $\mu \approx 1 \cdot 10^{-3}$[Pa · sec] where $\tau \ll 1 \approx 0.004$. In this regime, pressure propagates significantly slower than the solid field's response to change and solid inertia becomes negligible. The beam deformation reflects pressure-field evolution over time across the array of bellows, actuating them in sequence, first on the right half of the workspace, then the left.

The cyan dotted curve in Figure 4A shows what happens when the input pressure cycle is maintained, but the bellows are filled with air, $\mu \approx 2 \cdot 10^{-5}$[Pa · sec]. Now, the calculated timescale is two orders of magnitude higher and approaches unity $\tau \rightarrow 1 \approx 0.2$, that is, the pressure-field evolution timescale approaches that of the solid response. As a result, the pressure field is close to uniform within the entire bellow array, the connective configuration loses significance, and the actuator experiences almost pure axial extension and contraction, with all bellows experiencing uniform pressure in leading order.

Two additional insights raise from the spatially uniform case. First, as $\tau \gg 1$, the spatial pressure distribution approaches uniformity. Second, the measure of solid inertia involvement in the

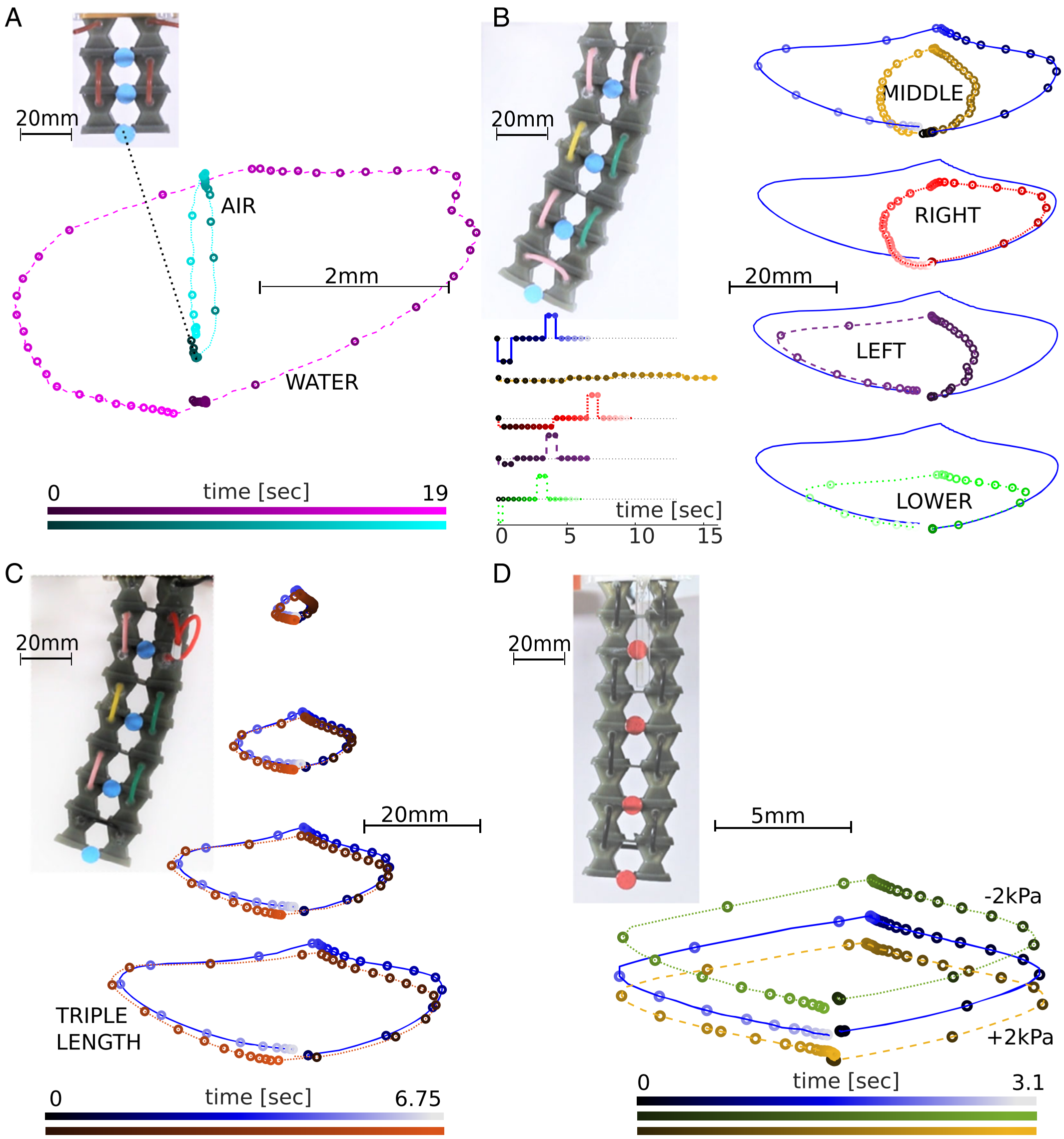

Figure 4. A) Change in a 4-bellow actuator cycle with internal fluid: water (- -) and air (.). The curves show the tracked path of the lower-most blue marker on the actuator. B–D) The blue curve shows the path of the 16-bellow actuator in a straight configuration with uniform tube length operated at ambient pressure gauge, also shown in Figure 3A. B) Operation over the middle- (-.-), right- (.), left- (- -), and lower- (..) workspace, due to a change in the pressure profile. The lower left insert shows relative amplitude of supply voltage to the syringe pump over time. C) Change in the actuator cycle when the top right tube has triple length (.). D) Vertical shift in the actuator cycle, due to changing absolute pressure gauge: $-2[kPa]$ (.) and $+2[kPa]$ (- -).

interaction increases as $t_s^*/t_i^* \gg 1$, where t_i^* is the characteristic timescale of the input signal defined as the minimum interval required to achieve input extrema pressure from gauge pressure baseline. Evaluating inertial involvement in our experiment, we estimate $t_i^* = 0.74$s and thus $t_s^*/t_i^* = 0.04$, thereby making solid inertia negligible. Last, it is important to note that the system's dynamic response to fluidic input pressure transients is governed in leading order by fluid viscosity corresponding to the viscous-elastic timescale t_f^*. Thus, the system acts as a low-pass filter, attenuating the frequency response from a cutoff frequency of the order $f_{\text{cutoff}} = O(10^1)/t_f^*[\text{Hz}]$, which drops as fluid viscosity increases.

3.3. Viscous-Elastic to Input Timescale Ratio

The pressure input profile is the most obvious form of control in this system, because it requires no physical change to the system or additional driver components. In Figure 4B and Movie S3, Supporting Information, we show how we can bias the actuator deflection to the middle, right, left, and lower part of the full workspace, by varying only the frequency, duty cycle, and amplitude of the input signal. Such differences may be useful to, for example, produce crouched gaits in the presence of obstacles or back- and front strokes for swimming robots.

3.4. Pressure-Field Diffusive Propagation

The viscous resistance affects the maximum flux throughout the actuator, and therefore has an effect on local deformation. In Figure 4C and Movie S4, Supporting Information, we demonstrate how a single change to the connective tubing—increasing the length of the second to third bellow tubing by three times—can reduce local mass flux by a third. This reduction in mass flow causes a local pressure concentration in the preceding bellow, that is, the first right-side bellow, resulting in a localized increase in contraction and expansion during an input pressure cycle, tilting the entire motion vertically down and to the left. In this way, localized irregularities can be superimposed on a desired actuation mode to tune cycle orientation. More information is provided in the last comment in Appendix Section B.3.7, Supporting Information.

3.4.1. Initial Gauge Pressure

A unique feature of closed fluid-driven systems is the ability to cycle the pressure gradient about an initial gauge that is different from ambient. By changing the gauge pressure around which the input pressure cycles, only the sum of pressure in a given cross-section $\overline{P}$ is changed, not the difference P'. As such this will generate the same motion pattern, just cycling around a different point along the actuator length. This concept is shown in practice in Figure 4D and Movie S5, Supporting Information.

3.5. Robot Implementation

To exemplify how viscous-driven soft actuators can be incorporated into a system, we further implemented a hexapod robot with six actuators, or "legs", driven in two sets of three by two syringe pumps carried on the back of the robot (Figure 2B). Note that we chose the initial gauge pressure in concert with the actuators that drive the change in pressure. Within a similar price range, more powerful electric motors which can overcome the increased resistance in the elastomer when the actuator is driven above or below ambient pressure are also heavier[32] and must cycle around a higher gauge pressure to meet the increased payload. To support the weight of the robot (734[g]), all legs are cycled around an initial gauge pressure of 140 kPa unloaded. The gauge pressure also affects the leg stiffness, a

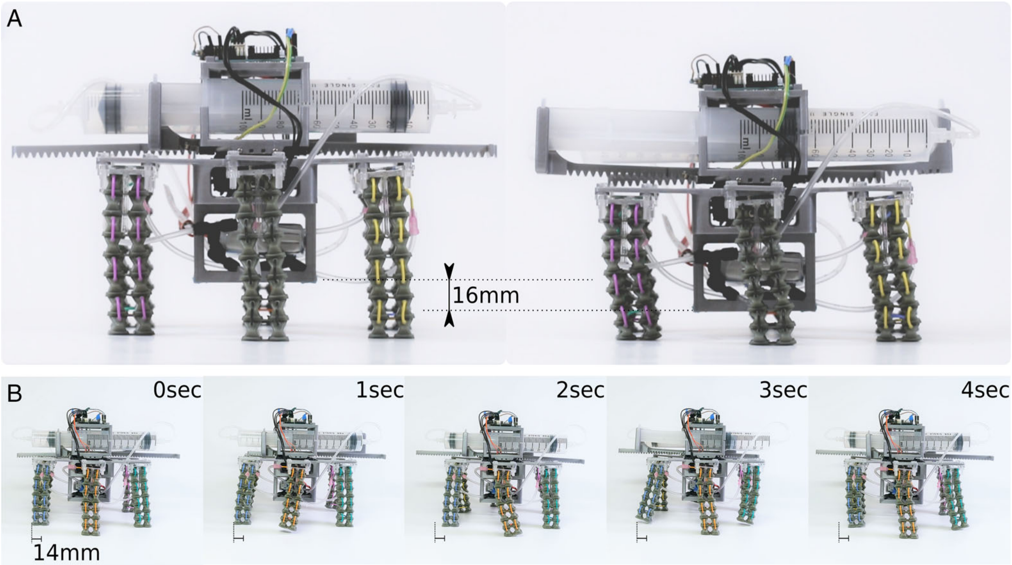

Figure 5. A) The absolute pressure can be changed in a hexapod robot to make it stand tall (left) or crouch (right). B) Snapshots from video accompanying the paper, in which the robot takes two steps forward.

feature that may be used in future studies to tune locomotion efficiency, robot payload, and stability depending on the surface terrain.

Figure 5A and Movie S6, Supporting Information, show how the actuators can be driven slowly to make the robot crouch—the legs compress to 85% of their original height. **Figure 5B** shows the robot walking over a horizontal smooth surface; more steps are shown in Movie S6, Supporting Information. The robot walks in a quasi-static mode, by balancing on three legs while lifting and moving the others, and can traverse a distance corresponding to its own body length ($\mathrm{BL} = 254\,[\mathrm{mm}]$) in $21\,[\mathrm{sec}]$, i.e., $0.05\,[\mathrm{BL/sec}]$; or $0.12\,[\mathrm{BL}] (= 14\,[\mathrm{mm}])$ per step. It is worth noting that this is relatively fast for an untethered, (non-combustion) legged robot.[4,33] For comparison, some of the most prominent fluid-driven soft-legged robots to date achieved $0.09\,[\mathrm{BL/sec}]$[19] $0.014\,[\mathrm{BL/sec}]$.[12]

4. Summary

In this work, we expanded existing knowledge on strategies for minimalistic control of underactuated soft robots. We focused on a simplified unit cell typical of soft FEAs, namely a closed series of elastomer bellows with fixed slender interconnections filled with fluid and arranged symmetrically around a neutral plane. We defined a theoretical framework to analyze the concerted relation between the three governing timescales: that of the input, the fluid, and the solid; identifying a void—a temporal domain in the field of soft robotics unexplored previous to this work. Within this goldilocks temporal domain, deformation patterns are driven by spatial viscous pressure variations generated by temporal gradients at the input that are on the same timescale as the fluid.

We detailed in theory and experiment the five principle mechanisms for generating these complex motions: 1) the spatial distribution of connected bellows, 2) the solid to fluid timescale ratio, 3) the viscous-elastic to input timescale ratio, 4) the pressure-field diffusive propagation, and the 5) initial gauge pressure. We showcased the utility of this work in a six-legged robot able to achieve a speed of $V = 0.05\,[\mathrm{BL/sec}]$; on par with existing, untethered, fluid-driven soft-legged walkers.

In summary, we showed that viscous-driven, nonuniform pressure distributions throughout the actuator can be harnessed to produce interchangeable, complex spatiotemporal motions in fixed-configuration FEAs with a single modulated pressure inlet. Essentially, this permits the designer to embed all or part of the control algorithm into the actuator morphology and material. While demonstrations in this article were limited to open loop operation, the two-way coupling between the solid and fluids also enables closed loop control, which we aim to address in future work. The contributed tool set of five principle mechanisms with their three timescales for input, fluid, and solid is key to unlocking more capable and competitive soft robots that fully harness their infinite degrees of freedom.

5. Experimental Section

Fluid Elastomer Actuators: The actuator used throughout the majority of the paper consisted of 16 bellows, connecting tubes, and a mechanical adapter that was mounted to a syringe pump. The bellows were produced on a Carbon 3D SLA printer from Sil-30, a flexible, tear-resistant silicone urethane. Each bellow contained a single bend to keep the form factor small while allowing for significant deformation. Each layer of the leg consisted of two open bellows mounted onto a lid with nested protrusions in an antagonistic fashion. Lids and bellows were bonded together using uncured Sil-30 and sealed by baking for 8 h at 120 [°C]. Each bellow was connected to up to two neighbors using 22 AWG silicone tubing and the inlet of the actuator was attached to a 20 G blunt tip luer-lock needle. Bonds were formed with cyanoacrylate super glue. The actuator was connected to a custom syringe pump by means of soft PVC Tygon B-44-3 tubing and a 3/32 ["] hose barb luer adapter.

The actuators were flexible in all directions and might lean sideways out of the plane of motion if externally loaded. To mitigate this issue in the hexapod robot, small rigid pillars were mounted along the side of the first two layers of bellows in each leg. A single actuator weighs approximately 31 g.

Model Parameters: The experimental setup consisted of an actuator of length $l_\mathrm{s} = 0.109\,[\mathrm{m}]$, height $h_\mathrm{s} = 0.03\,[\mathrm{m}]$, and width $w_\mathrm{s} = 0.02\,[\mathrm{m}]$, made up of $n = 16$ bellows. The SIL-30 material had a Young's modulus of $E = 1.8\,[\mathrm{MPa}]$ and density of $\rho_\mathrm{s} \approx 950\,[\mathrm{kg\,m^{-3}}]$. The actuator's solid mass fraction was $f_\mathrm{m} \approx 0.47$, resulting in actuator mass per unit length of $m = \rho_\mathrm{s}(w_\mathrm{s} h_\mathrm{s}),\ f_\mathrm{m} = 0.269\,[\mathrm{kg\,m^{-1}}]$. Due to the nontrivial elastomer distribution in the typical cross section, the section area and second moment of inertia were approximated as $a = h_\mathrm{s} w_\mathrm{s} \approx 6 \cdot 10^{-4}\,[\mathrm{m^2}]$ and $I = (w_\mathrm{s} h_\mathrm{s}^3)/12 \approx 4.5 \cdot 10^{-8}\,[\mathrm{m^4}]$. We then multiplied the results by correction coefficients for cross-sectional extension and bending stiffness compared to a solid rectangular beam, $f_\mathrm{e} \approx 0.53$ and $f_i \approx 0.55$ respectively; these were calculated numerically in a cantilever setup using COMSOL 5.5 basic Solid Mechanics module. Last, the fabricated bellows height, width, and length were $(h_\mathrm{b}, w_\mathrm{b}, l_\mathrm{b}) = (0.010, 0.012, 0.018)\,[\mathrm{m}]$, the radius of the connective tubes was $r_\mathrm{c} = 3.25 \cdot 10^{-4}\,[\mathrm{m}]$, and the total length of tubes was $l = 0.6\,[\mathrm{m}]$.

We experimentally measured five coupling coefficients quantifying the fluid–structure interaction including 1) the change in bellow cross section per unit pressure $\partial a_{p1}/\partial p = 3.413 \cdot 10^{-9}\,[\mathrm{m^2}/Pa]$, 2) the change in actuator slope per cross section per normalized pressure difference $\partial\psi/\partial(p'/E) = 10.266\,[\mathrm{Rad/1}]$, 3) the change in actuator length per cross section per normalized pressure sum $\partial\zeta/\partial(\overline{p}/E) = 0.047\,[\mathrm{m/1}]$, 4) the change in bellow cross section per normal force resultant $\partial a_1/\partial N_\mathrm{e} \approx 0.03 \cdot 10^{-5}\,[\mathrm{m^2/N}]$, and 5) the change in bellow cross-section per moment resultant $\partial a_1/\partial M_\mathrm{e} \approx 1.2 \cdot 10^{-6}\,[\mathrm{m^2/Nm}]$. See Appendix Section C, Supporting Information, for more information.

Drive Circuitry: The individual legs and the hexapod robot were all driven by a custom backpack equipped with an Arbotix-M controller, one 11.1 [V] 450 [mAh] LiPo battery, and two syringe pumps controlling two sets of three legs, respectively. Each syringe pump consisted of a gear-rack system (18 gear teeth, pitch diameter 29.6 [mm]) and a 100 [mL] syringe, driven by a Dynamixel AX-18A servo with a stall torque of 1.8 [Nm] and a no load speed of 97 [rpm]. Sensors included limit switches to prevent overextension and a Phidgets 1140-1 pressure sensor. The backpack frame was printed in lightweight PLA for minimum payload; the full backpack weighs 510 [g], including the two servos which weigh 112 [g] each. To increase stability, the backpack was configured such that the lightweight syringes and electronics mounted on top and the heavier batteries sat low between the legs for stability. Each set of legs were connected to the syringe using soft PVC Tygon B-44-3 tubing, T-connectors, and a 3/32 ["] hose barb luer adapter. Each leg was mechanically attached to the backpack with four nylon bolts; washers with a thickness up to 4 [mm] were used to angle the legs outward for added stability.

Supporting Information

Supporting Information is available from the Wiley Online Library or from the author.

Acknowledgements

This work was sponsored by the Army Research Laboratory and was accomplished under Cooperative Agreement (CA) W911NFT16T2T0008, and the National Science Foundation Awards CNS-2042411, a Packard Fellowship for Science and Engineering, an Aref and Manon Lahham faculty fellowship, and GETTYLABS. The views and conclusions contained in this document are those of the authors and should not be interpreted as representing the official policies, either expressed or implied, or the Army Research Laboratory or the US Government. The US Government is authorized to reproduce and distribute reprints for government purposes notwithstanding any copyright notation herein.

Conflict of Interest

The authors declare no conflict of interest.

Data Availability Statement

The data that support the findings of this study are available from the corresponding author upon reasonable request.

Keywords

fluid-driven elastomer actuators, morphological intelligence, soft robotics

Received: October 3, 2022
Revised: December 15, 2022
Published online:

---

[1] T. Ashuri, A. Armani, R. Jalilzadeh Hamidi, T. Reasnor, S. Ahmadi, K. Iqbal, *Biomed. Eng. Lett.* **2020**, *10*, 369.
[2] J. Hughes, U. Culha, F. Giardina, F. Guenther, A. Rosendo, F. Iida, *Front. Rob. AI* **2016**, *3*, 69.
[3] P. Polygerinos, N. Correll, S. A. Morin, B. Mosadegh, C. D. Onal, K. Petersen, M. Cianchetti, M. T. Tolley, R. F. Shepherd, *Adv. Eng. Mater.* **2017**, *19*, 1700016.
[4] S. I. Rich, R. J. Wood, C. Majidi, *Nat. Electron.* **2018**, *1*, 102.
[5] L. Hines, K. Petersen, G. Z. Lum, M. Sitti, *Adv. Mater.* **2017**, *29*, 1603483.
[6] F. Connolly, P. Polygerinos, C. J. Walsh, K. Bertoldi, *Soft Rob.* **2015**, *2*, 26.
[7] I. D. Walker, D. M. Dawson, T. Flash, F. W. Grasso, R. T. Hanlon, B. Hochner, W. M. Kier, C. C. Pagano, C. D. Rahn, Q. M. Zhang, *Unmanned Ground Vehicle Technology VII*, Vol. *5804*, Defense and Security, Orlando, Florida, United States **2005**, pp. 303–314.
[8] J. W. Booth, J. C. Case, E. L. White, D. S. Shah, R. Kramer-Bottiglio, in *2018 IEEE Int. Conf. Soft Robotics (RoboSoft)*, IEEE, Piscataway, NJ **2018**, pp. 25–30.
[9] D. Yang, B. Mosadegh, A. Ainla, B. Lee, F. Khashai, Z. Suo, K. Bertoldi, G. M. Whitesides, *Adv. Mater.* **2015**, *27*, 6323.
[10] M. A. Robertson, J. Paik, *Sci. Rob.* **2017**, *2*, 9.
[11] J. D. Greer, L. H. Blumenschein, A. M. Okamura, E. W. Hawkes, in *2018 IEEE Int. Conf. Robotics and Automation (ICRA)*, IEEE, Piscataway, NJ **2018**, pp. 4165–4172.
[12] D. Drotman, S. Jadhav, D. Sharp, C. Chan, M. T. Tolley, *Science Rob.* **2021**, *6*, 51.
[13] Y. Matia, T. Elimelech, A. D. Gat, *Soft Rob.* **2017**, *4*, 126.
[14] Y. Matia, A. D. Gat, https://arxiv.org/abs/1812.08717 (accessed: April 2021).
[15] C. C. Futran, S. Ceron, B. C. Mac Murray, R. F. Shepherd, K. H. Petersen, in *2018 IEEE Int. Conf. Soft Robotics (RoboSoft)*, IEEE, Piscataway, NJ **2018**, pp. 473–478.
[16] L. Salem, B. Gamus, Y. Or, A. D. Gat, *Soft Rob.* **2020**, *7*, 76.
[17] N. Vasios, A. J. Gross, S. Soifer, J. T. Overvelde, K. Bertoldi, *Soft Rob.* **2020**, *7*, 1.
[18] M. Wehner, R. L. Truby, D. J. Fitzgerald, B. Mosadegh, G. M. Whitesides, J. A. Lewis, R. J. Wood, *Nature* **2016**, *536*, 451.
[19] M. Tolley, R. F. Shepherd, K. C. Galloway, R. J. Wood, G. M. Whitesides, *Soft Rob.* **2014**, *1*, 3.
[20] K. Suzumori, S. Endo, T. Kanda, N. Kato, H. Suzuki, in *Proc. 2007 IEEE Int. Conf. Robotics and Automation*, IEEE, Piscataway, NJ **2007**, pp. 4975–4980.
[21] K. Suzumori, A. Koga, F. Kondo, R. Haneda, *Robotica* **1996**, *14*, 493.
[22] K. Suzumori, S. Iikura, H. Tanaka, in *Proc. 1991 IEEE Int. Conf. Robotics and Automation*, IEEE Computer Society, Piscataway, NJ **1991**, pp. 1622–1623.
[23] R. F. Shepherd, F. Ilievski, W. Choi, S. A. Morin, A. A. Stokes, A. D. Mazzeo, X. Chen, M. Wang, G. M. Whitesides, *Proc. Natl. Acad. Sci.* **2011**, *108*, 20400.
[24] B. Mosadegh, P. Polygerinos, C. Keplinger, S. Wennstedt, R. F. Shepherd, U. Gupta, J. Shim, K. Bertoldi, C. J. Walsh, G. M. Whitesides, *Adv. Funct. Mater.* **2014**, *24*, 2163.
[25] K. McDonald, A. Rendos, S. Woodman, K. A. Brown, T. Ranzani, *Adv. Intell. Syst.* **2020**, *2*, 2000139.
[26] T. J. Jones, E. Jambon-Puillet, J. Marthelot, P.-T. Brun, *Nature* **2021**, *599*, 229.
[27] R. F. Shepherd, A. A. Stokes, J. Freake, J. Barber, P. W. Snyder, A. D. Mazzeo, L. Cademartiri, S. A. Morin, G. M. Whitesides, *Angew. Chem., Int. Ed.* **2013**, *52*, 2892.
[28] R. F. Shepherd, A. A. Stokes, R. Nunes, G. M. Whitesides, *Adv. Mater.* **2013**, *25*, 6709.
[29] Y. Matia, A. D. Gat, *Soft Rob.* **2015**, *2*, 42.
[30] R. Deimel, O. Brock, in *2013 IEEE Int. Conf. Robotics and Automation*, IEEE, Piscataway, NJ **2013**, pp. 2047–2053.
[31] B. Gamus, L. Salem, E. Ben-Haim, A. D. Gat, Y. Or, *IEEE Trans. Rob.* **2017**, *34*, 81.
[32] A. Hughes, B. Drury, *Electric Motors and Drives: Fundamentals, Types and Applications*, Newnes, Oxford, UK, and Boston, USA **2019**.
[33] M. Calisti, G. Picardi, C. Laschi, *J. R. Soc. Interface* **2017**, *14*, 20170101.